

SPATIALLY RESOLVED *SPITZER* IRS SPECTROSCOPY OF THE CENTRAL REGION OF M82

P. BEIRÃO,¹ B. R. BRANDL,¹ P. N. APPLETON,² B. GROVES,¹ L. ARMUS,³ N. M. FÖRSTER SCHREIBER,⁴
J. D. SMITH,⁵ V. CHARMANDARIS,⁶ AND J. R. HOUCK⁷

Received 2007 February 7; accepted 2007 November 27

ABSTRACT

We present high spatial resolution (~ 35 pc) 5–38 μm spectra of the central region of M82, taken with the *Spitzer* Infrared Spectrograph. From these spectra we determined the fluxes and equivalent widths (EWs) of key diagnostic features, such as the [Ne II] 12.8 μm , [Ne III] 15.5 μm , and H₂ S(1) 17.03 μm lines, and the broad mid-IR polycyclic aromatic hydrocarbon (PAH) emission features in six representative regions and analyzed the spatial distribution of these lines and their ratios across the central region. We find a good correlation of the dust extinction with the CO 1–0 emission. The PAH emission follows closely the ionization structure along the galactic disk. The observed variations of the diagnostic PAH ratios across M82 can be explained by extinction effects, within systematic uncertainties. The 16–18 μm PAH complex is very prominent, and its EW is enhanced outward from the galactic plane. We interpret this as a consequence of the variation of the UV radiation field. The EWs of the 11.3 μm PAH feature and the H₂ S(1) line correlate closely, and we conclude that shocks in the outflow regions have no measurable influence on the H₂ emission. The [Ne III]/[Ne II] ratio is on average low, at ~ 0.18 , and shows little variations across the plane, indicating that the dominant stellar population is evolved (5–6 Myr) and well distributed. There is a slight increase of the ratio with distance from the galactic plane of M82, which we attribute to a decrease in gas density. Our observations indicate that the star formation rate has decreased significantly in the last 5 Myr. The quantities of dust and molecular gas in the central area of the galaxy argue against starvation and for negative feedback processes, observable through the strong extraplanar outflows.

Subject headings: galaxies: individual (M82) — galaxies: starburst — infrared: galaxies

Online material: color figures

1. INTRODUCTION

M82 (NGC 3034) is an irregular galaxy located at 3.3 Mpc (Freedman & Madore 1988) in the M81 group. It is the closest starburst galaxy, seen nearly edge-on, with an inclination angle of about 80° . At infrared wavelengths it is the brightest galaxy on the sky, with a total infrared luminosity of $3.8 \times 10^{10} L_\odot$ (Colbert et al. 1999). Most of its luminosity originates from the inner 500 pc, hosting intense starburst activity presumably triggered by a tidal interaction with M81 (e.g., Yun et al. 1993). Evidence for this interaction comes from the H I streams that connect M81 to all three (M82, NGC 3077, and NGC 2976) peculiar members of the inner M81 group (Appleton et al. 1981; Yun et al. 1994). Recent deep optical images also revealed stars associated with the H I bridge between M81 and M82 (Sun et al. 2005).

At the distance of M82, 1'' corresponds to 15 pc, which allows spatially resolved studies of the starburst region. Evidence of a stellar bar ~ 1 kpc long is shown by near-infrared studies (e.g., Telesco et al. 1991; Larkin et al. 1994) and mid-infrared [Ne II] 12.8 μm and millimetric CO emission studies (Lo et al. 1987). According to Larkin et al. (1994) and Achtermann & Lacy (1995),

there is a rotating ring of ionized gas at a radius of ~ 85 pc and on the inner side of a ring of molecular gas at ~ 210 pc. Two possible spiral arms were also identified by Shen & Lo (1995) and Mayya et al. (2005) at radii of ~ 125 and ~ 400 pc. The starburst of M82 drives a bipolar mass outflow out to several kiloparsecs perpendicular to the plane of the galaxy, which is especially evident in X-ray and H α (Bregman et al. 1995; Shopbell & Bland-Hawthorn 1998; Lehnert et al. 1999; Cappi et al. 1999; Strickland et al. 2004). Dust has also been detected in the outflow region (Alton et al. 1999; Heckman et al. 2000; Hoopes et al. 2005; Engelbracht et al. 2006). The star-forming regions of M82 are predominantly clustered in the volume enclosed by the molecular gas ring, indicated by the H II region tracers such as the [Ne II] 12.8 μm line and the mid and far-infrared continuum emission (Telesco et al. 1991; Walter et al. 2002; Larkin et al. 1994; Achtermann & Lacy 1995; Lipsky & Plavchan 2004). Near-infrared hydrogen recombination lines also arise in these regions, but they are a more ambiguous tracer of star formation, as they can also be excited by shocks, although these are unlikely to dominate.

Near-infrared integral field spectroscopy and *ISO* SWS mid-infrared spectroscopy by Förster Schreiber et al. (2001) allowed a detailed modeling of starburst activity in the central region of M82 (Förster Schreiber et al. 2003a). These models are consistent with the occurrence of starburst activity in two successive episodes, about 10 and 5 Myr ago, each lasting a few million years. However, the spatial studies by Förster Schreiber et al. (2001) and others covered only near-infrared wavelengths. The large aperture of the *ISO* SWS provided a continuous 2.4–45 μm spectrum but covered the whole central region of M82. ISOCAM CVF data (Förster Schreiber et al. 2003b) provided better spatial resolution, but the spectra only had a spatial resolution of $R \sim 40$ and were shortward of 15 μm .

¹ Leiden Observatory, Leiden University, P. O. Box 9513, 2300 RA Leiden, Netherlands.

² NASA Herschel Science Center, California Institute of Technology, Pasadena, CA 91125.

³ Spitzer Science Center, California Institute of Technology, Pasadena, CA 91125.

⁴ Max-Planck-Institut für extraterrestrische Physik, Garching, Germany.

⁵ Steward Observatory, University of Arizona, Tucson, AZ 85721.

⁶ IESL/Foundation for Research and Technology-Hellas, GR-71110 Heraklion, Greece; and Chercheur Associé, Observatoire de Paris, F-75014, Paris, France.

⁷ Astronomy Department, Cornell University, 219 Space Sciences Building, Ithaca, NY 14853.

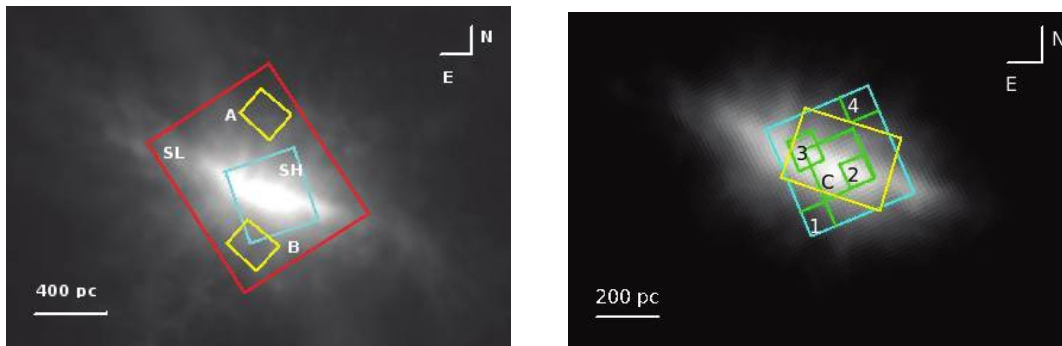


FIG. 1.—*Left*: Overlay of SL (red) and SH (blue) coverages and selected low-resolution extraction regions on an IRAC $8\ \mu\text{m}$ image. Regions A and B, represented in yellow, are regions where LL ($14\text{--}35\ \mu\text{m}$) spectra were extracted. *Right*: Zoom-in of the IRAC $8\ \mu\text{m}$ image with an overlay of the SH map area in blue and the selected regions (green) from where the SH+SL spectra were extracted. The ISO SWS aperture used in the $12\text{--}27\ \mu\text{m}$ range by Förster Schreiber et al. (2001) is also overlaid in yellow on the image. Both figures are in logarithmic scaling.

Engelbracht et al. (2006) published *Spitzer* IRS low-resolution spectra of a $1'$ wide strip along the minor axis of M82, intersecting the disk at the eastern side. The spectra, taken as part of the SINGS Legacy project, were combined with *Spitzer* 8 and $24\ \mu\text{m}$ images, and show that the emission by polycyclic aromatic hydrocarbons (PAHs) and H_2 molecules extends far out from the disk (to 6 kpc) in both directions. Engelbracht et al. (2006) suggest that the filamentary aromatic-dominated emission either represents dust expelled from the galaxy as a result of a powerful nuclear superwind or indicates that dust in the halo is being lit up by the starburst, perhaps coexisting with the extensive warm H_2 molecules. They suggest that this halo dust is probably a leftover from the interaction with M81.

In this paper we present mid-IR spectral maps at unsurpassed sensitivity and spatial resolution of the central $\sim 0.5\ \text{kpc}^2$ of M82, covering the main contributors to the bolometric luminosity of the galaxy. Our goal is to provide a spatial and spectrally detailed description of the physical conditions within the central $\sim 500\ \text{pc}$ of M82, to help us to gain an insight on the evolution of the starburst activity in this region. This involves the study of the distribution of the radiation field, gas density, and the physical properties of PAHs. Of particular interest are the spatial variations of the fine-structure lines, the excitation of the molecular hydrogen, and the distribution of the PAH molecules. In § 2 we describe the observations and data reduction; in § 3 we present the data; and in § 4 we discuss the scientific results, followed by our conclusions in § 5.

2. OBSERVATIONS AND DATA REDUCTION

The observations were made with the Infrared Spectrograph (IRS)⁸ spectrometer (Houck et al. 2004) on board the *Spitzer Space Telescope*, under the IRS guaranteed time observing program. The data were taken on 2005 June 6 using the IRS “mapping mode” in all four modules: Short-High (SH; $10\text{--}19\ \mu\text{m}$) and Long-High (LH; $14\text{--}38\ \mu\text{m}$) provide $R \sim 600$, while Short-Low (SL; $5\text{--}14\ \mu\text{m}$) and Long-Low (LL; $14\text{--}38\ \mu\text{m}$) give $R \sim 60\text{--}130$. Each of the SL and LL modules are further divided into two subslits, which correspond to diffraction orders: SL1 ($7.5\text{--}14\ \mu\text{m}$), SL2 ($5\text{--}7.5\ \mu\text{m}$), LL1 ($20\text{--}38\ \mu\text{m}$), and LL2 ($14\text{--}20\ \mu\text{m}$). The SH map consists of 30 pointings with four cycles each, and each subsequent pointing is offset by half a slit width parallel to the slit and about one-third of the slit length along the slit. The SH map covers an area of $28'' \times 23''$. The LH data consists of

12 pointings, with five cycles each, covering an area of $38'' \times 33''$. The offsets are equivalent to the SH map. The SL data consists of 120 pointings, with two cycles each, covering an area over the M82 central region of $55.5'' \times 57''$. The LL data consists of 22 pointings with two cycles each. Both SL and LL maps follow the same offsetting scheme as SH. Because of the high brightness of M82 it was unavoidable that the LL1 data became saturated near the center of M82, but the LL2 data are still usable. Figure 1 (*left*) shows the areas covered by the IRS SL, LH, and SH maps overlaid on the IRAC $8\ \mu\text{m}$ image from Engelbracht et al. (2006). The total integration times range from 12 s (for SL exposures) to 31 s (for LH exposures). Due to issues concerning the extraction, the LH spectra were not used in this analysis. The boxes labelled “A” and “B” are the regions where the complete low-resolution (SL+LL) spectra were extracted.

The data were processed with version 13.2 of the *Spitzer* reduction pipeline (ver. 14 for LL). Observations taken at each position were combined into spectral cubes using CUBISM (Smith et al. 2007a), an IDL-based software package designed to combine spectral mapping data sets into three-dimensional spectral cubes. Bad pixels in the basic calibrated data (BCD) spectra were manually flagged and then automatically discarded when rebuilding the cube. Spectra from off-source positions 1 kpc to the northeast of the nucleus were used to subtract the background from the low-resolution spectra. For the high-resolution spectra we did not subtract a background, since there was no suitable “sky” spectrum available and the high source fluxes strongly dominate any background emission. The spectral analysis was done using SMART (Higdon et al. 2004) and PAHFIT (Smith et al. 2007b).

3. ANALYSIS

On the basis of the SH spectral map coverage we defined six subregions for which we extracted the spectra from SL and SH with CUBISM. The location of these regions is shown in Figure 1 (*right*) overlaid on the IRAC $8\ \mu\text{m}$ image from Engelbracht et al. (2006). The ISO aperture is also shown to illustrate the increase in spatial resolution obtained with the *Spitzer* IRS. Regions 2 and 3 coincide with the peaks of the [Ne II] emission, regions 1 and 4 are offset to both sides of the galactic disk, the slightly larger region C covers the nominal center of the galaxy, and the final region corresponds to the entire area mapped with the SH spectrograph. The exact coordinates and sizes are listed in Table 1.

Figure 2 shows the SL ($5\text{--}14\ \mu\text{m}$) and SH ($10\text{--}19\ \mu\text{m}$) spectra extracted for these six regions. The noise is negligible and the spectra exhibit the classical features of starburst galaxies (Brandl et al. 2006), such as strong emission features of the

⁸ The IRS was a collaborative venture between Cornell University and Ball Aerospace Corporation funded by NASA through the Jet Propulsion Laboratory and the Ames Research Center.

TABLE 1
CHARACTERISTICS OF THE SELECTED REGIONS

Coordinates	Region 1	Region 2	Region 3	Region 4	Center	Total	Region A	Region B
R.A. (J2000.0)	9 55 52.42	9 55 50.63	9 55 52.74	9 55 50.22	9 55 51.19	9 55 51.32	9 55 52.17	9 55 52.68
Decl. (J2000.0).....	+69 40 32.1	+69 40 45.6	+69 40 48.5	+69 40 58.60	+69 40 46.8	+69 40 45.30	+69 41 12.5	+69 40 22.2
Size.....	6.8" × 6.8"	6.8" × 6.8"	6.8" × 6.8"	6.8" × 6.8"	11.3" × 11.3"	24.9" × 24.9"	14.8" × 20.3"	14.8" × 20.3"

NOTE.—Units of right ascension are hours, minutes, and seconds, and units of declination are degrees, arcminutes, and arcseconds.

PAHs, fine-structure lines, and emission from molecular hydrogen, in addition to the broad silicate absorption features around 9.7 and 18 μm , with an underlying continuum of very small grain emission. The 5–38 μm wavelength range contains many important diagnostic lines, such as [Ar II] 6.99 μm , [Ar III] 8.99 μm , [S IV] 10.51 μm , [Ne II] 12.81 μm , [Ne III] 15.56 μm , and [S III] 18.71 μm . All of the detected features are labeled in Figure 2. The fluxes and ratios of the most relevant fine-structure and H₂ emission lines are listed in Table 2. These lines were measured using Gaussian fits to the line and linear fits to the local continuum. The [Ne II] line was measured after subtracting the 12.6 μm PAH feature. [S IV] at 10.5 μm is hard to detect on regions 1 and 4 due to the low signal-to-noise ratio (S/N), and [Ar III], at 8.99 μm , is too close to the 8.6 μm PAH feature to be detected in a low-resolution spectrum. Due to saturation of the LL1 module and extraction issues of the LH spectra, we could not measure the [S III] 33.6 μm line.

Numerous PAH emission features are easily detectable in our spectra. The fluxes and equivalent widths (EWs) of the strongest features at 6.2, 7.7, 8.6, 11.3, 12.6, and 14.2 μm , as well as the 16–18 μm complex are listed in Table 3. Their values were derived using PAHFIT (Smith et al. 2007b), an IDL tool that decomposes low-resolution spectra of PAH emission sources using a physically motivated model. This model includes starlight, thermal dust continuum, resolved dust features and feature blends, prominent emission lines, and dust extinction. In our case we merged SL and SH spectra in order to have one spectrum for each region with the widest wavelength coverage possible. Weaker PAH features at 5.2, 5.6, 12.0, and 13.55 μm are present in the spectra in Figure 2 but are not used further in this paper. In Figure 3 we present an example of a fit to a combined SL+SH spectrum of region 2. In the overall spectrum (*green*) we distinguish the continuum component (*red*), PAH component (*blue*), ionic lines (*purple*), and dust absorption (*dashed line*).

Silicate absorption affects mainly the wavelength interval from 7–12 μm . In PAHFIT we have the option to include or exclude silicate absorption, and the difference between these two cases can be up to 50% in flux of the 11.3 μm feature. In § 4.3 we discuss the methods to estimate the magnitude and distribution of extinction. In addition, there is a significant difference in the 11.3 μm flux between the SH and SL spectra, which can also

reach 50%. This difference can be attributed to a poor fit to the silicate absorption feature in SH, as this module only covers wavelengths >10 μm . In this paper we use the SH+SL measurements for this reason and to include the 17 μm complex.

We also extracted combined SL+LL spectra (5–38 μm) from two 15" × 20" regions, A and B (see Fig. 1, *left*), at a distance of 200 pc above and below the galactic plane of M82, where saturation did not compromise the LL measurements. Their positions are listed in Table 1. The spectra from regions A and B were virtually identical in shape, and an average of these spectra is shown in Figure 4. The spectrum is clearly dominated by strong PAH emission features and a steeply rising continuum, characteristic of classical starburst galaxies (e.g., Brandl et al. 2006). The wiggles observed longward of 20 μm are fringes that originate from interferences in the detector substrate material. At the low spatial resolution presented by the LL modules, we cannot see any unusual features in the SL+LL spectra of regions A and B. Also, as the LL1 slit is saturated at the central region of M82, we cannot extract any full low-resolution spectra of this region, connecting it to regions A and B. For these reasons, we do not make further analysis of LL1 module spectra in this paper.

4. RESULTS AND DISCUSSION

The main gain of our observations over previous work on the starburst in M82 is the availability of spatially resolved mid-IR spectroscopy of the central region. Despite their overall similarity, the spectra show distinct variations in the relative strengths of the spectral features, in particular in the neon fine-structure lines and PAH features. These variations and their physical causes are described in the following sections.

4.1. The Morphology of the Starburst Region

The discovery of a series of compact radio supernova remnants along the galactic plane of M82, extending over 600 pc (Kronberg et al. 1985; Muxlow et al. 1994), is an indication of very recent and presumably ongoing star formation. The detection of the ionic high-excitation lines [Ne III] and [S IV] confirms the presence of very young massive stars in M82. Ratios using ionic lines of the same species and different ionization potentials such as [Ne III]/[Ne II], [S IV]/[S III], and [Ar III]/[Ar II] are a useful measure of the hardness and intensity of the radiation field and

TABLE 2
MAIN EMISSION-LINE STRENGTHS IN UNITS OF $10^{-19} \text{ W cm}^{-2}$

Region	[Ar II] 6.99 μm	[S IV] 10.5 μm	[Ne II] 12.8 μm	[Ne III] 15.6 μm	[S III] 18.7 μm	H ₂ S(1) 17.0 μm	H ₂ S(2) 12.3 μm	T [S(1)–S(2)] (K)	[Ne III]/[Ne II]	
1.....	0.30 ± 0.03	0.04 ± 0.01	1.04 ± 0.03	0.22 ± 0.01	0.38 ± 0.01	0.12 ± 0.01	0.07 ± 0.01	1.71 ± 0.46	381 ± 44	0.21 ± 0.02
2.....	7.82 ± 0.23	0.31 ± 0.01	25.3 ± 0.9	3.42 ± 0.09	8.5 ± 0.19	0.23 ± 0.04	0.25 ± 0.03	0.92 ± 0.30	586 ± 117	0.13 ± 0.01
3.....	5.77 ± 0.10	0.33 ± 0.01	18.4 ± 0.4	3.58 ± 0.06	5.92 ± 0.18	0.25 ± 0.04	0.27 ± 0.03	0.93 ± 0.28	583 ± 109	0.19 ± 0.02
4.....	0.44 ± 0.02	0.03 ± 0.01	1.73 ± 0.04	0.36 ± 0.01	0.66 ± 0.02	0.08 ± 0.003	0.06 ± 0.003	1.33 ± 0.13	439 ± 31	0.21 ± 0.02
Center.....	17.1 ± 0.47	0.72 ± 0.08	55.4 ± 0.97	8.53 ± 0.15	18.6 ± 0.37	0.51 ± 0.07	0.67 ± 0.07	0.76 ± 0.21	700 ± 129	0.15 ± 0.01
Total.....	44.8 ± 1.49	2.16 ± 0.13	141.2 ± 3.10	23.6 ± 0.38	49.0 ± 0.83	2.53 ± 0.09	2.47 ± 0.11	1.02 ± 0.09	536 ± 32	0.17 ± 0.02

TABLE 3
MAIN PAH FEATURE STRENGTHS AS MEASURED WITH PAHFIT

Region	6.2 μm	7.7 μm	8.6 μm	11.3 μm	12.6 μm	14.2 μm	17 μm complex	$F(17 \mu\text{m complex})/$ $F(6.2 \mu\text{m})$	$F(17 \mu\text{m complex})/$ $F(11.3 \mu\text{m})$
	Flux ^a EW ^b								
1.....	8.9 \pm 0.1 0.308	29.9 \pm 0.1 0.254	6.2 \pm 0.1 0.437	10.9 \pm 0.1 2.27	6.0 \pm 0.1 2.06	0.62 \pm 0.01 2.13	4.2 \pm 0.03 1.97	0.47	0.39
2.....	154.7 \pm 0.1 1.10	528.0 \pm 0.2 0.866	99.3 \pm 0.1 0.848	77.9 \pm 0.1 0.660	64.5 \pm 0.1 0.734	6.1 \pm 0.1 0.717	34.6 \pm 0.1 0.753	0.22	0.44
3.....	136.3 \pm 0.1 0.827	478.2 \pm 0.2 0.884	83.6 \pm 0.1 0.865	73.7 \pm 0.1 0.784	57.2 \pm 0.1 0.877	5.5 \pm 0.1 0.850	29.1 \pm 0.1 0.720	0.21	0.39
4.....	13.3 \pm 0.1 0.390	49.6 \pm 0.1 0.320	11.3 \pm 0.1 0.575	15.7 \pm 0.1 1.86	7.7 \pm 0.1 1.52	0.67 \pm 0.10 1.30	7.6 \pm 0.1 2.16	0.57	0.48
Center.....	375.0 \pm 0.2 1.22	1320.0 \pm 0.5 0.991	242.40 \pm 0.5 0.937	202.5 \pm 0.6 0.758	156.3 \pm 0.3 0.791	14.3 \pm 0.1 0.750	99.0 \pm 0.2 0.907	0.26	0.49
Total	1158.0 \pm 1.0 1.00	4121.7 \pm 3.4 1.00	743.9 \pm 1.5 1.00	736.0 \pm 1.7 1.00	535.8 \pm 0.7 1.00	52.2 \pm 0.2 1.00	327.8 \pm 0.5 1.00	0.28	0.45

^a Flux in units of $10^{-19} \text{ W cm}^{-2}$. The quoted errors are only the PAHFIT fit residuals. EWs are normalized to the EWs for the whole SH slit.

^b EW in units of μm .

radiation density, and are therefore sensitive to the presence of young massive stars.

Our measurements of the $[\text{Ne III}]/[\text{Ne II}]$ ratio are shown in Table 2 for each of the six selected regions. We find $0.13 \leq [\text{Ne III}]/[\text{Ne II}] \leq 0.21$, with a median of $[\text{Ne III}]/[\text{Ne II}] = 0.18$, which is consistent with the spatially integrated ratio of $[\text{Ne III}]/[\text{Ne II}] = 0.16 \pm 0.04$ determined by Förster Schreiber et al. (2001). These values are 30% lower than the average value of 0.26 for the *ISO* SWS sample of starburst galaxies (Thornley et al. 2000) and more than an order of magnitude below the value of 8.5 found in the center of NGC 5253 (Beirão et al. 2006), a low-metallicity starburst galaxy at about the same distance as M82.

Other ratios, such as $[\text{S IV}]/[\text{S III}]$ and $[\text{Ar III}]/[\text{Ar II}]$, could be used to confirm the results on the $[\text{Ne III}]/[\text{Ne II}]$. However, as mentioned in § 3, our measurements of $[\text{S IV}]$ in regions 1 and 4 have large errors from noise, and $[\text{Ar III}]$, at $8.99 \mu\text{m}$, is too close to the $8.6 \mu\text{m}$ PAH feature to be measured accurately from the low-resolution spectrum, precluding the use of these ratios.

The *Spitzer* IRS spectral maps allow a study of the spatial variation of the radiation field, based on the $[\text{Ne III}]/[\text{Ne II}]$ ratio. Due to the presence of several luminous star clusters in the central region, one might expect strong variations of $[\text{Ne III}]/[\text{Ne II}]$ between regions. In Figure 5 we present spectral maps of the two strongest neon emission lines and a ratio map, overlaid by the $12 \mu\text{m}$ continuum contours from Achtermann & Lacy (1995). For both line maps, CUBISM was used to subtract a fitted continuum map from a total line+continuum map at the same wavelength on a pixel-by-pixel basis. The $[\text{Ne II}]$ emission in the top map shows two peaks to either side of the nucleus, a weaker and a stronger peak, which correspond to the east and west peaks, respectively, in Achtermann & Lacy (1995). After a close inspection, we identify the strong west peak in our maps with the two continuum emission peaks. The east and west $[\text{Ne II}]$ emission peaks are identified as a “ring” of ionized gas in Achtermann & Lacy (1995). The morphology of the $[\text{Ne II}]$ emission follows the $\text{Br}\gamma$ emission in Satyapal et al. (1997) and Förster Schreiber et al. (2001). The $[\text{Ne III}]$ map also reveals two emission peaks at the same positions, but with the eastern peak brighter relative to the western peak.

The bottom map in Figure 5 presents the $[\text{Ne III}]/[\text{Ne II}]$ ratio. The ratio varies from 0.08–0.27 throughout the map. The lower value corresponds to the location of the westernmost clusters, and there is a significant increase in the ratio farther out from the

galactic plane of M82, from 0.15 to 0.27. Statistical 1σ errors are $\sim 15\%$ and arise mostly from baseline determination errors. The gray line represents the direction of the X-ray outflow observed in M82 (Strickland et al. 1997, 2004). It originates from the nucleus (*plus sign*) and is perpendicular to the plane of the galaxy. The peak of X-ray emission is offset from the outflow axis by 30 pc. Although the gradient in the $[\text{Ne III}]/[\text{Ne II}]$ ratio does follow the outflow axis, it appears offset by $5''$ to the east, associated with the eastern cluster.

The overall morphology of the ionizing radiation in the region as revealed by the spectral maps seems to be in agreement with ground observations of the continuum and $[\text{Ne II}]$ emission by Achtermann & Lacy (1995). However, the $[\text{Ne III}]/[\text{Ne II}]$ ratio varies only by a factor of 3 throughout the region, and these variations do not correspond to the position of the emission peaks. An increase of the $[\text{Ne III}]/[\text{Ne II}]$ ratio is observed farther out from the galactic plane, but due to the limited spatial coverage of the map, we cannot determine if this increase is connected to the outflows. The origins of the observed emission morphology and the variation of the $[\text{Ne III}]/[\text{Ne II}]$ ratio are discussed in the following subsection.

4.2. Origins of the Variation of the Radiation Field

The $[\text{Ne III}]/[\text{Ne II}]$ ratio measures the hardness of the radiation field, which is a function of stellar age and metallicity, and is often parameterized by the effective temperature, T_{eff} , and the radiation intensity as measured by the ionization parameter U .⁹ Given the strength of the $[\text{Ne II}]$ and $[\text{Ne III}]$ lines in M82, and their proximity in wavelength, which minimizes the effects of extinction, $[\text{Ne III}]/[\text{Ne II}]$ is the most reliable measure of the hardness of the radiation field. With the help of starburst models, it is possible to use the $[\text{Ne III}]/[\text{Ne II}]$ ratio to estimate the ages of the massive clusters in the region.

Observations with the *ISO* SWS have been used previously for this purpose. Förster Schreiber et al. (2001) determined a spatially integrated ratio of $[\text{Ne III}]/[\text{Ne II}] = 0.16$ for the inner 500 pc of M82. Using the photoionization code CLOUDY and

⁹ U is defined as $U = Q/4\pi R^2 n_{\text{H}} c$, where Q is the production rate of ionizing photons from the stars, R is the distance between the ionizing cluster and the illuminated gas cloud, n_{H} is the hydrogen number density of the gas, and c is the speed of light.

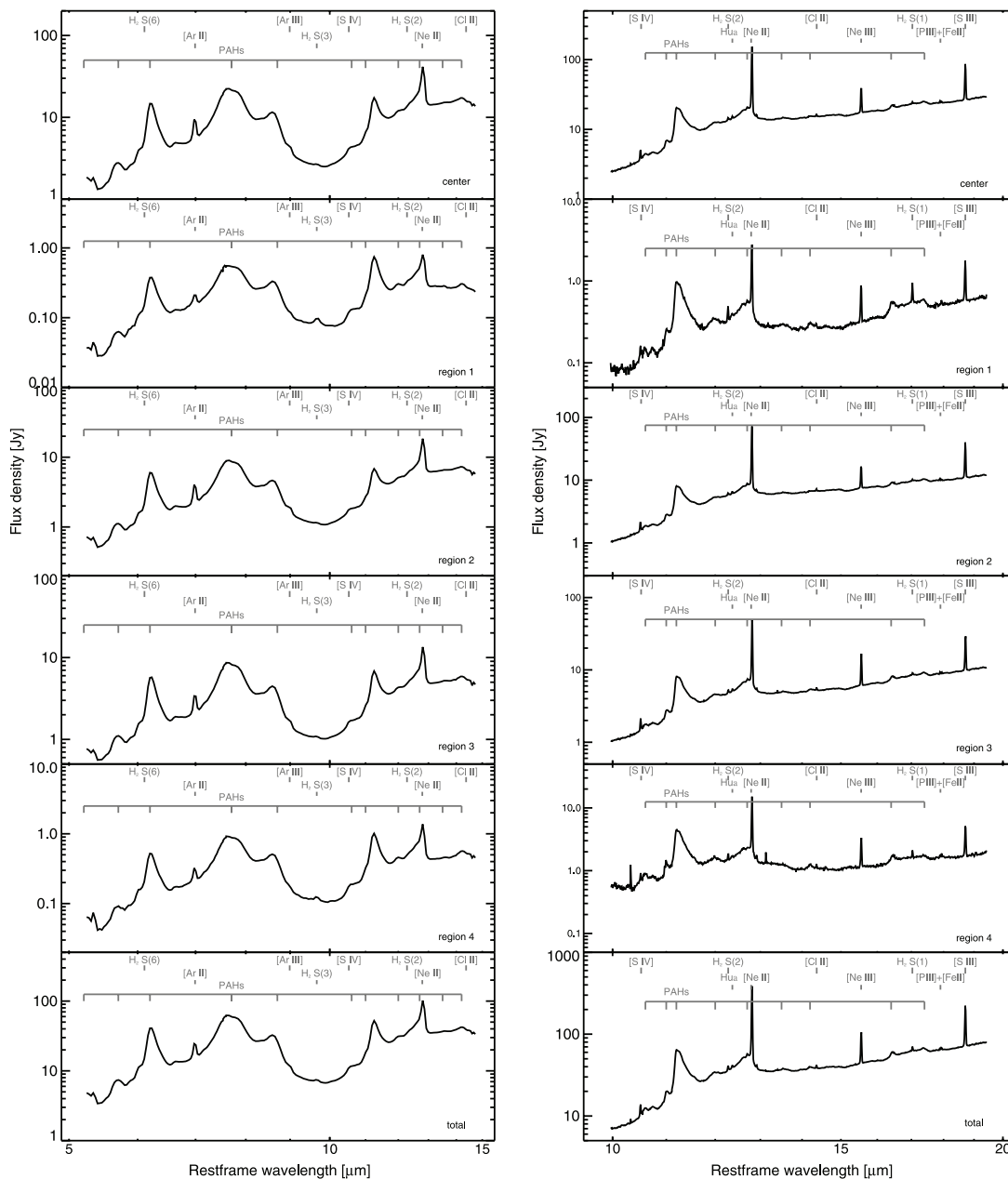


FIG. 2.— SL (left) and SH (right) spectra of the six selected regions within the central starburst region of M82. The “total” region corresponds to the total SH map in Fig. 1. [See the electronic edition of the *Journal* for a color version of this figure.]

solar metallicity stellar atmosphere models by Pauldrach et al. (1998), Förster Schreiber et al. (2001) modeled the variations of line ratios with T_{eff} . Adopting an electron density $n_e = 300 \text{ cm}^{-3}$ and an ionization parameter $\log U = -2.3$, Förster Schreiber et al. (2003a) found for the *ISO* value for $[\text{Ne III}]/[\text{Ne II}]$ an effective temperature of $37,400 \pm 400 \text{ K}$ and a burst age of 4–6 Myr. Other observed ratios were also modeled, such as $[\text{Ar III}]/[\text{Ar II}]$ and $[\text{S IV}]/[\text{S III}]$, giving similar T_{eff} values (within uncertainties). Independent estimations of cluster ages were done at longer wavelengths. Colbert et al. (1999) analyzed far-infrared spectra from the *ISO* LWS and fitted line ratios to a combined H II region and PDR model. Their best-fit model is an instantaneous starburst of 3–5 Myr old massive stars, in agreement with Förster Schreiber et al. (2003a).

If the infrared emission peaks correspond to massive clusters of stars, we can determine their ages from the measured $[\text{Ne III}]/$

$[\text{Ne II}]$ ratio and compare them with the above results, using the photoionization models by Snijders et al. (2007). As input, Snijders et al. (2007) used massive cluster spectra modeled with Starburst99, assuming a Salpeter IMF, $M_{\text{up}} = 100 M_{\odot}$, $M_{\text{low}} = 0.2 M_{\odot}$, and a gas density of 100 cm^{-3} . This value of gas density is a factor of 3 lower than $\log U = -2.3$, the Förster Schreiber et al. (2001) value, but this discrepancy has a small effect on the $[\text{Ne III}]/[\text{Ne II}]$ ratio. Figure 6 shows the results for a range of ionization parameters. The selected regions are represented by horizontal lines. The value of $\log U = -2.3$ derived by Förster Schreiber et al. (2001) corresponds to a ionization front speed of $q = 1.6 \times 10^8 \text{ cm s}^{-1}$. For a typical value of q , the ages of the clusters in each region range from 5 to 6 Myr, in agreement with the previously determined burst ages. These clusters dominate the central region of M82 and may be similar to those observed farther out in M82 in the optical, studied in detail by Smith et al.

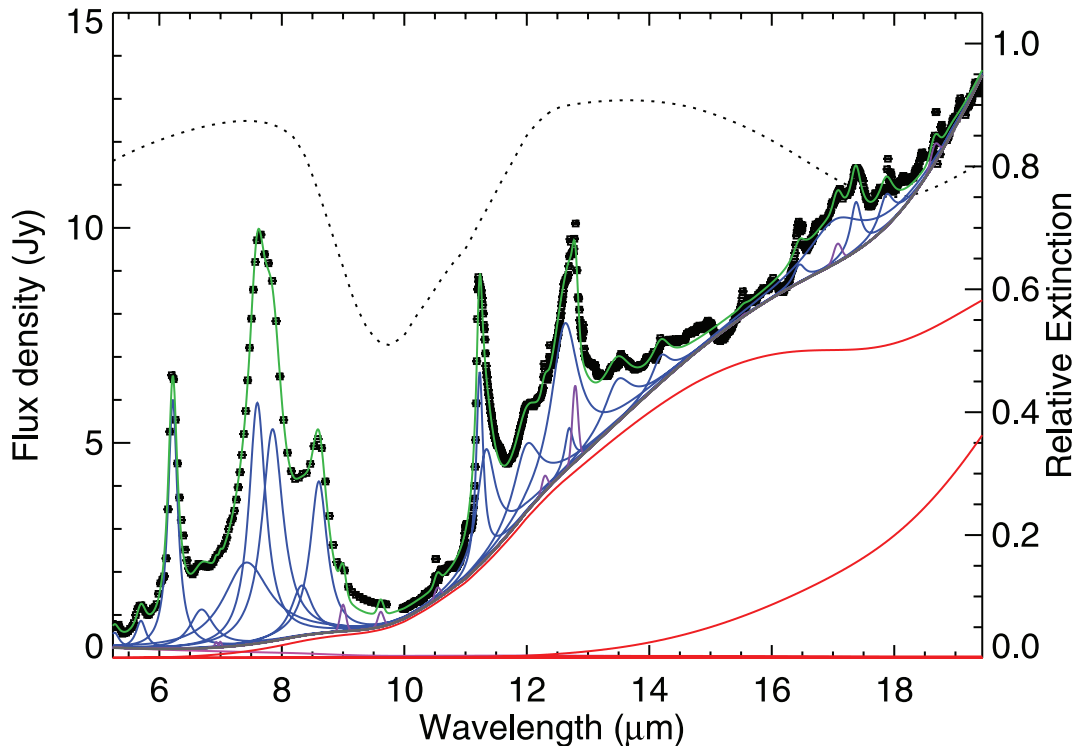


FIG. 3.— Decomposition of SL+SH spectrum of region 2. Red solid lines represent the thermal dust continuum components, the thick gray line the total continuum, blue lines are dust features, while the violet peaks are atomic and molecular spectral lines. The dotted black line indicates the fully mixed extinction which affects all components, with axis at right. The solid green line is the full fitted model, plotted on the observed flux intensities and uncertainties.

(2006) using the *HST* ACS, which were found to have an average age of 6.4 ± 0.5 Myr.

As shown in Figure 5, the $[\text{Ne III}]/[\text{Ne II}]$ ratio increases from 0.15 to 0.27 with increasing distance from the galactic plane of M82. This is counterintuitive, as one might expect a harder radiation field at the location of the most luminous regions along the plane. Away from the plane, a decrease of gas density relative to the number of ionizing photons leads to an increase of the ionization parameter, which then causes an increase of the $[\text{Ne III}]/[\text{Ne II}]$ ratio, as discussed in Thornley et al. (2000). Indeed, Figure 6 shows that the $[\text{Ne III}]/[\text{Ne II}]$ scales with the ionization parameter. The variation we observe in the $[\text{Ne III}]/[\text{Ne II}]$ ratio implies a variation by a factor of 5 in the ionization parameter. This is equivalent to saying that the gas density decreases 5 times

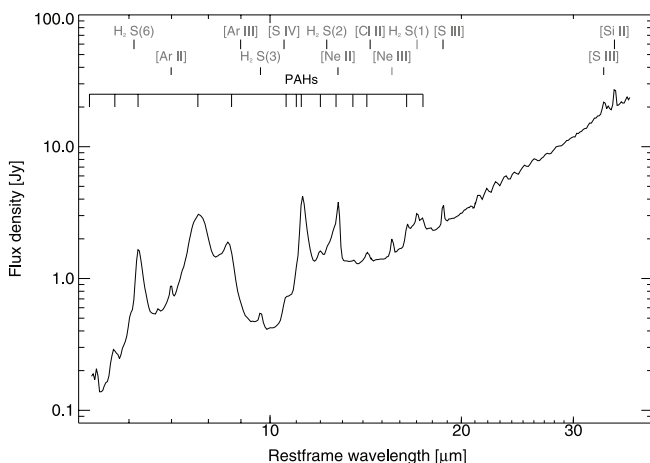


FIG. 4.— Average of the 5–38 μm low-resolution IRS spectra of the regions A and B, located approximately 200 pc above and below the galactic plane of M82.

faster than the radiation field, which decreases as $\sim R^{-2}$, with R being the distance to the ionization source. Shocks could also contribute to the increase of the $[\text{Ne III}]/[\text{Ne II}]$ ratio in the outflow region, but in § 4.5 we show this effect to be minimal. This hypothesis could be tested using the $[\text{S III}] 18.6 \mu\text{m}/[\text{S III}] 33.6 \mu\text{m}$ ratio. Unfortunately, due to the problems reported in § 2, we could not derive an accurate flux for the $[\text{S III}] 33.6 \mu\text{m}$ line in both LL and LH spectra.

It is important to emphasize that even at higher angular resolution, the $[\text{Ne III}]/[\text{Ne II}]$ ratio in M82 remains quite low for an active starburst. We would have expected a larger variation, with higher ratios locally corresponding to younger clusters and lower ratios elsewhere. A comparison with the *ISO* SWS sample of starburst galaxies (Thornley et al. 2000) shows that it is actually lower than most starbursts, despite being closer and better resolved. The low $[\text{Ne III}]/[\text{Ne II}]$ ratio could be caused by an aged stellar population in which starburst activity ceased more than half a dozen megayears ago—although this possibility seems unlikely given the large amounts of molecular gas still present at the center of M82. An edge-on view of the galaxy could also contribute to the low variation of $[\text{Ne III}]/[\text{Ne II}]$ ratio.

As a comparison, we examined the $4.5'' \times 4.5''$ area with the highest $[\text{Ne III}]$ flux (Fig. 5), comparing the measured $[\text{Ne II}]$ and $[\text{Ne III}]$ luminosities with the models to determine the enclosed stellar mass. A single super star cluster of 5 Myr would have a cluster mass of $10^6 M_{\odot}$, which is twice the mass of the super star cluster in NGC 5253 (Turner et al. 2003). A single cluster in a $4.5'' \times 4.5''$ area would correspond to a cluster number density of $\sim 200 \text{ kpc}^{-2}$, which is comparable to the cluster density found in the fossil starburst region of M82 by de Grijs et al. (2001).

While the average age of the starburst population in M82 appears to be ~ 5 Myr, ongoing star formation (≤ 1 Myr) could possibly be obscured by recent contributions of older stellar populations (> 5 Myr) to the neon ratio. Considering this possibility,

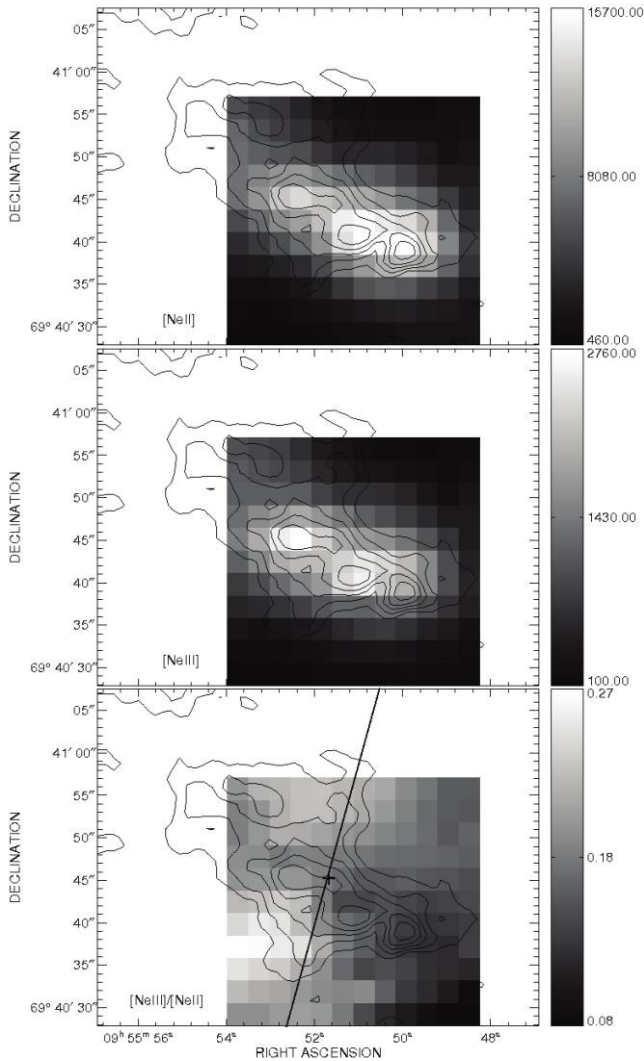


FIG. 5.— Spectral maps in the $[\text{Ne II}]$ (top), $[\text{Ne III}]$ (middle), and $[\text{Ne III}]/[\text{Ne II}]$ (bottom) lines from the IRS SH module, with contour overlays of the $12\ \mu\text{m}$ continuum emission from Achtermann & Lacy (1995). The regions shown are $\sim 26'' \times 26''$. At the bottom map, the line is the direction of the of the X-ray outflow, which is perpendicular to the plane of the galaxy. The cross represents the nucleus.

we explore the region with the highest $[\text{Ne III}]$ flux, a strong indicator of the presence of O stars, as an illustrative case to set an upper limit on the ongoing star formation in M82. This region has a $[\text{Ne III}]/[\text{Ne II}]$ of ~ 0.10 , with a total $[\text{Ne III}]$ luminosity of $1.41 \times 10^6 L_{\odot}$. Assuming $\sim 1.6 \times 10^8\ \text{cm s}^{-1}$, a typical young cluster of 1 Myr has $[\text{Ne III}]/[\text{Ne II}] \sim 5$ and can contribute $\sim 50\%$ to the total $[\text{Ne III}]$ luminosity, or $\sim 2.5\%$ per mass relative to the older 5–6 Myr old population. This means that the 1 Myr old population only emits $\sim 5\%$ of the total $[\text{Ne II}] + [\text{Ne III}]$ luminosity of the older 5–6 Myr old population. Even as an upper limit, this value indicates that the activity of the starburst has substantially declined relative to the high star formation rate that existed 5 Myr ago.

Despite the reduced starburst activity, the presence of CO emission all over the central region (Fig. 7) shows that the starburst in M82 still has a large gas reservoir, as pointed out by Thornley et al. (2000) and Förster Schreiber et al. (2003a). It appears therefore unlikely that the starburst activity ceased because of lack of fuel. On the other hand, negative feedback mainly through strong stellar winds and supernovae explosions can play an important role in

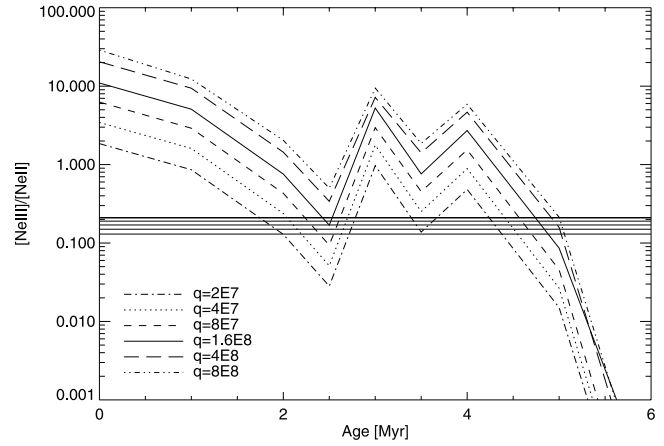


FIG. 6.— Effect of the cluster age on the $[\text{Ne III}]/[\text{Ne II}]$ ratio. The model curves are computed for a cluster of $10^6 M_{\odot}$, assuming Salpeter IMF, $M_{\text{up}} = 100 M_{\odot}$, and $M_{\text{low}} = 0.2 M_{\odot}$. Each curve represents a different ionization parameter, and the solid curve is the one that approaches the value found by Förster Schreiber et al. (2001) $\log U = -2.3$. The horizontal lines indicate the $[\text{Ne III}]/[\text{Ne II}]$ for each selected region, from region 1 to region 4. The first dip in $[\text{Ne III}]/[\text{Ne II}]$ represents the ageing of the stellar population, after which WR stars are produced, increasing the $[\text{Ne III}]/[\text{Ne II}]$ ratio. The dip at 6 Myr occurs as most massive stars die through supernova explosions.

determining the star formation rate in starbursts. Förster Schreiber et al. (2003a) calculated a feedback timescale of 1–10 Myr, which is in good agreement with the age of the older super star clusters in the central region of M82.

In summary, we find that $[\text{Ne III}]/[\text{Ne II}]$ ratio is low on average and increases with distance from the galactic plane of M82. The increase can be explained by an increase of the ionization parameter through a drop in gas density. The low $[\text{Ne III}]/[\text{Ne II}]$ ratio indicates that the dominant population consists of older clusters (>5 Myr). We cannot rule out the presence of younger clusters in the central region, but they would be at a much reduced rate ($<5\%$) of star formation compared to previous epochs. The large amount of molecular gas still present in the central region argues against a starvation of starburst activity due to lack of gas. Instead, we believe that negative feedback processes are responsible for the observed decline in the star formation rate.

4.3. Extinction

One of the most noticeable features in the spectra in Figure 2 is the absorption feature at 9–11 μm caused by silicate grains.

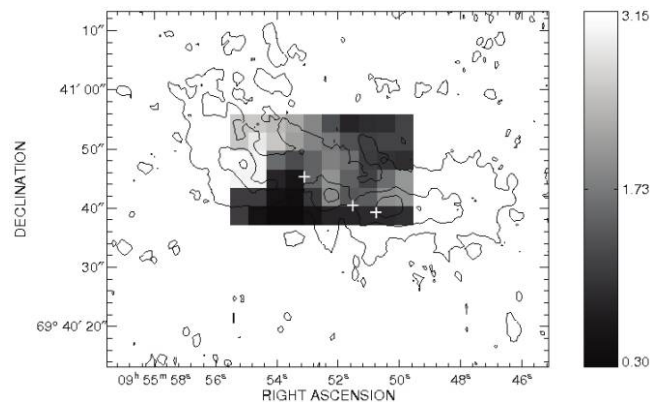


FIG. 7.— Map of $\tau_{9.8}$, determined from a simple continuum fit to the SL spectra, with overlay of CO 1–0 emission contours from Shen & Lo (1995). The crosses indicate the $[\text{Ne II}]$ emission peaks. The image was rotated by 55° and interpolated.

This feature can be extremely deep especially in ULIRGS (e.g., Spoon et al. 2007) and affects the observed fluxes of spectral lines and features in this region. The strength of this feature is characterized by the optical depth at $9.8 \mu\text{m}$ ($\tau_{9.8}$), assuming a simple geometrical dust distribution. For our analysis it is important to estimate the intensity of this feature and its spatial variation in order to investigate its influence on the PAH strengths, which we discuss in the following subsections.

To study the distribution of $\tau_{9.8}$ in the SL region, we selected an area of 20×12 pixels in the center of the SL1 map. Within that area we extracted spectra from 60 spatial resolution elements (2×2 pixels each).

The apparent optical depth $\tau_{9.8}$ is then estimated from the ratio of the interpolated continuum to the observed flux at $9.8 \mu\text{m}$. For the central region of M82, $\tau_{9.8}$ ranges from 0.3 to 3.1, assuming foreground screen attenuation. We built an extinction map of 10×6 resolution elements from the simple-fit method, which is shown in Figure 7. The qualitative distribution of $\tau_{9.8}$ observed in this figure is very similar to the qualitative results from the PAHFIT fitting method. There is a good correlation between the $\tau_{9.8}$ distribution and the CO 1–0 emission, indicating that dust and molecular gas coincide in this region. The enhanced $\tau_{9.8}$ in the northwest region of the map indicates an increase of silicate dust above the galactic plane.

For an independent, and possibly more accurate, estimate of $\tau_{9.8}$, we used PAHFIT on 15 SL+LL1 spectra ($5\text{--}20 \mu\text{m}$), each corresponding to four resolution elements fitted only with SL. With the PAHFIT method, $\tau_{9.8}$ ranges from 0 to 2.52, with a median is 1.34.

The combined SL+LL spectrum is necessary to better constrain the parameters in PAHFIT. Fitting only SL spectra with PAHFIT can result in large errors in the calculation of $\tau_{9.8}$. Unfortunately, due to saturation at wavelengths longward of $20 \mu\text{m}$, we have an insufficient spatial coverage of LL data in the central region. In addition, the LL slits are $\sim 10''$ wide, providing low spatial resolution.

For the higher spatial resolution, we used the simple method described by Spoon et al. (2007) to estimate $\tau_{9.8}$. In this method we approximate the mid-IR continuum at $9.8 \mu\text{m}$ by a power-law fit to the flux pivots at 5.5 and $14.5 \mu\text{m}$, avoiding the PAH emission features.

The values derived from both SL+LL and simple-fit methods agree qualitatively well, but in regions where $\tau_{9.8} < 1$, the difference between the two methods is greater than a factor of 2. Using a mixed attenuation law with $A_v/\tau_{9.8} = 16.6$ (Rieke & Lebofsky 1985), the range of $\tau_{9.8}$ corresponds to $0 < A_v < 41.8$ for the SL+LL method. The values of $\tau_{9.8}$ from the power-law interpolation method give $5.0 < A_v < 51.5$. These values are in agreement with Förster Schreiber et al. (2001), who derive $23 < A_v < 45$ for their selected regions in M82 covering an area closer to the infrared peaks.

We conclude that both methods, besides their significant uncertainties in the magnitude of $\tau_{9.8}$, have consistently revealed significant variations in the amount of dust extinction across the central region. These variations are strong enough to affect the following interpretation of PAH features.

4.4. Variations of PAH Emission Features

Polycyclic aromatic hydrocarbons (PAHs) are thought to be responsible for a series of broad emission features that dominate the mid-infrared spectra of starbursts (e.g., Peeters et al. 2004b). They are observed in a diverse range of sources, with their strongest emission originating in photodissociation regions (PDRs), the interfaces between H II regions and molecular clouds.

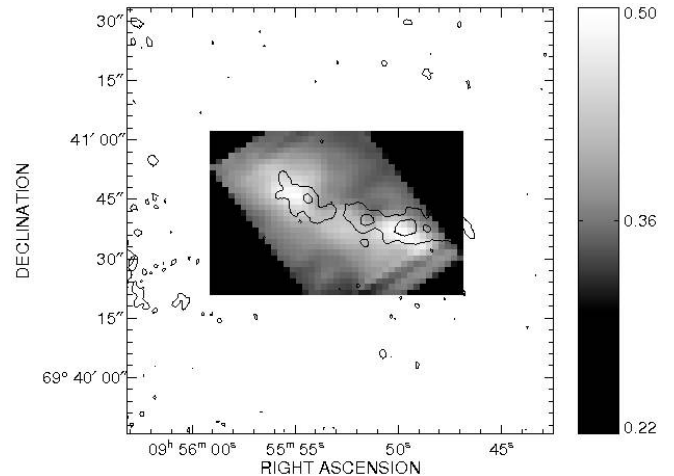


FIG. 8.—IRS spectral map of the PAH ratio $6.2/11.3 \mu\text{m}$, with overlay of CO 1–0 emission contours from Shen & Lo (1995). The map is in logarithmic scaling. This map was done using CUBISM maps of baseline-subtracted flux at $6.0\text{--}6.5$ and $11\text{--}11.7 \mu\text{m}$.

The relative strength of the different PAH bands is expected to vary with the size and the ionization state of the PAH molecule (Draine & Li 2001, 2007). Observations of Galactic sources (e.g., Verstraete et al. 1996; Joblin et al. 1996; Vermeij et al. 2002) have shown that the relative strengths of individual PAH features depend on the degree of ionization: C–C stretching modes at 6.2 and $7.7 \mu\text{m}$ are predominantly emitted by PAH cations, while the C–H out-of-plane bending mode at $11.3 \mu\text{m}$ arises mainly from neutral PAHs (Draine & Li 2001). Thus, the ratios $6.2/11.3$ and $7.7/11.3 \mu\text{m}$ may be used as indicators of the PAH ionization state. Joblin et al. (1996) have found that the $8.6/11.3 \mu\text{m}$ ratio can also be linked to variations in the charge state of the emitting PAHs, which is supported by laboratory experiments (Hudgins & Allamandola 1995). Smith et al. (2007b) found band strength variations of factors of 2–5 among normal galaxies.

Studies of PAHs in M82 have been done previously using ISO. Observations with ISOCAM (Förster Schreiber et al. 2003b) revealed a decrease in the $6.2/7.7 \mu\text{m}$ ratio and an increase in the $8.6/11.3 \mu\text{m}$ PAH ratio from the nucleus outward along the galactic plane. The observations also showed a good spatial correlation of the $8.6/11.3 \mu\text{m}$ ratio with the CO (1–0) emission. These ratio variations are attributed to real differences in the variation of physical characteristics of PAHs across M82, specifically a higher degree of PAH ionization within the most intense starburst sites.

We use CUBISM to build maps of ratios of PAH features that exist in the $6\text{--}14 \mu\text{m}$ SL spectra. The $7.7 \mu\text{m}$ feature is split between the two SL orders, and the $8.6 \mu\text{m}$ feature is largely influenced by the $7.7 \mu\text{m}$ feature, making the local continuum determination difficult. For these reasons the $6.2 \mu\text{m}$ feature map was chosen to be compared to the $11.3 \mu\text{m}$ feature map. In Figure 8 we present the $6.2/11.3 \mu\text{m}$ PAH ratio map, overlaid with the CO (1–0) contours from Shen & Lo (1995).

Obviously, the distribution of the $6.2/11.3 \mu\text{m}$ PAH ratio correlates well with the molecular ring defined by the CO (1–0) map. The molecular emission forms two lobes ~ 200 pc from the nucleus, whereas the ionized emission is concentrated around the nucleus, in the regions where the [Ne II] and [Ne III] emissions peak.

However, the $6.2/11.3 \mu\text{m}$ PAH ratio may be affected by extinction. Comparing the CO emission with the extinction map in Figure 7 and with the PAH ratio map, we see that they correlate

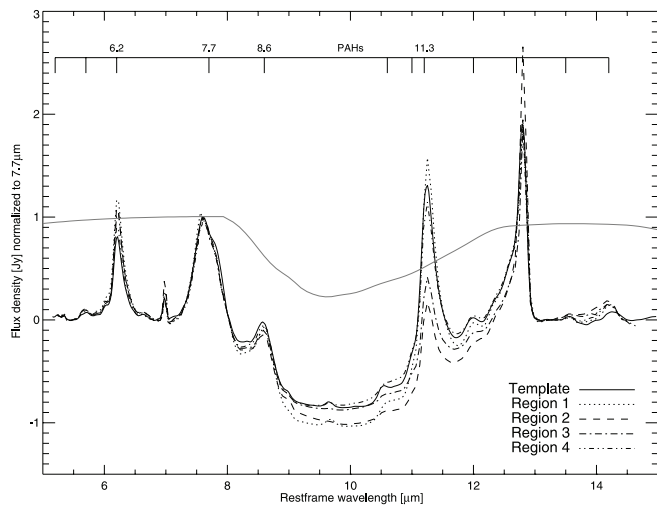


FIG. 9.— Baseline subtracted IRS spectra of the selected regions from Fig. 1. The gray line is the Chiar & Tielens (2006) extinction law, applied to a normalized flux of 1.75, and assuming $\tau_{9.8} = 2$.

well. Hence, we investigate the effects of extinction on the observed PAH ratios in the next subsection.

4.4.1. Influence of Silicate Absorption on PAH Ratios

The fluxes of the PAH bands at 6.2, 7.7, 8.6, and 11.3 μm are all affected by dust absorption. However, the 11.3 μm is significantly more affected by the 9.8 μm silicate feature than the 6.2 μm feature, which affects the measured PAH ratio shown in Figure 8. To illustrate this influence, we show in Figure 9 the baseline-subtracted spectra of the selected regions around the nucleus in M82, normalized to the flux at 7.7 μm to emphasize the relative flux variations of the 11.3 μm PAH feature. The gray line is the Chiar & Tielens (2006) extinction law, applied to a normalized flux of 1.75, assuming $\tau_{9.8} = 2$. For this figure, the baseline was removed by subtracting a second-order polynomial fitted to the following wavelengths: 5.5, 6.8, 8.0, 13.2, and 14.5 μm . These wavelengths were chosen to avoid the silicate feature at 10 μm and the PAH features. The effect of extinction on the 8.6 and 11.3 μm PAH features is similar, meaning that the 8.6/11.3 μm ratio could possibly be used to study PAH ionization with minimal concern for extinction, as the difference in flux correction between 8.6 and 11.3 μm is $\sim 15\%$. However, the 8.6 μm feature is influenced by the broad PAH feature at 7.7 μm , which makes local continuum fitting more difficult compared to the 6.2 μm feature.

Figure 9 suggests that the variations of PAH feature ratios involving the 11.3 μm feature will be heavily affected by extinction, contributing to the distribution of the 6.2/11.3 μm PAH ratio in Figure 8. The 7.7 μm PAH feature is affected by extinction to a similar level as the 6.2 μm feature, as shown in Figure 9. Draine & Li (2001) use the 6.2/7.7 μm ratio for PAH size diagnostic and 11.3/7.7 μm for a PAH ionization state diagnostic. Variations of these ratios reflect real variations of the physical properties of PAHs in M82 only if their variations are not due to extinction effects. Figure 10 presents the 6.2/7.7 and 11.3/7.7 μm PAH ratios calculated from PAHFIT measurements of the same subregions as in the extinction map. The data in Figure 10 are corrected for extinction. We took the average of the extinction methods (continuum fit method and the PAHFIT fit on SL+LL1 spectra; see § 4.3) for correction. The points are dispersed between the tracks representing totally ionized and neutral PAH populations, and the error bars show the average of the differ-

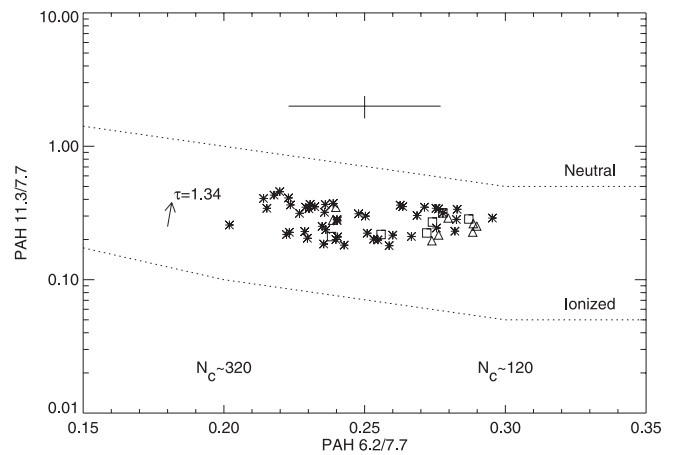


FIG. 10.— The 6.2/7.7 μm PAH ratio vs. the 11.3/7.7 PAH ratio, for the same subregions as in the absorption map in Fig. 7. The triangles are points from the areas where $[\text{Ne III}]/[\text{Ne II}] > 0.22$, and the squares are points from the areas where $[\text{Ne III}]/[\text{Ne II}] < 0.13$. Error bars represent average uncertainties, related to extinction correction and fitting uncertainties. The arrow represents the effect of a silicate absorption feature with $\tau_{9.8} = 1.34$. The tracks represent the ratios of a population of neutral and ionized PAHs.

ence between the extinctions derived by the two methods. The triangles are points from the areas where $[\text{Ne III}]/[\text{Ne II}] > 0.24$ in the $[\text{Ne III}]/[\text{Ne II}]$ map from Fig. 5. These are regions with harder radiation field, where a greater number of ionized PAH are expected to be observed. The squares are points from areas in the map where $[\text{Ne III}]/[\text{Ne II}] < 0.13$. To preserve the clarity of the plot, only the error bars at these points are represented, as they are typical for all the points. The arrow represents the effect on the ratios of a silicate absorption feature with $\tau_{9.8} = 1.34$, which is the median optical depth for the region as explained in § 4.3.

The 11.3/7.7 μm PAH ratios are dispersed between 0.2 and 0.5. However, the error bar can account for this dispersion, demonstrating how silicate absorption can affect the diagnostic of PAH ionization state based on this ratio, on scales of the size of the IRS resolution elements, ~ 35 pc. This implies that the average variations in the ionization state of the grains are relatively small on scales of 35 pc. These results are to be compared to SINGS results, in which the 11.3/7.7 μm PAH ratio is found to lie within the same range as that in the central region of M82 for galaxies dominated by H II regions (Smith et al. 2006).

The 6.2/7.7 μm ratio varies between ~ 0.2 and ~ 0.3 . This is well within the range of 0.2–0.4 reported by Smith et al. (2007b) for SINGS galaxies dominated by H II regions. We observe no significant difference in the 6.2/7.7 μm ratio between regions with a high $[\text{Ne III}]/[\text{Ne II}]$ ratio and regions with a lower $[\text{Ne III}]/[\text{Ne II}]$ ratio. Extinction and fitting errors affect the 6.2/7.7 μm ratio by only $\sim 1\%$, and errors from fitting residuals from PAHFIT amount to less than 2%. However, there are significant uncertainties arising from the continuum fitting by blackbody curves with effective temperatures between 35–300 K. Modifying the number of blackbody components and their temperatures results in changes in the PAH ratios in excess of 8%–12%. The horizontal error bar represents the average uncertainty of 10%.

The range of 6.2/7.7 μm ratios implies an environment composed of a warm ionized medium and photodissociation regions (PDRs; Draine & Li 2001). The dispersion in the data could reflect a real variation of this ratio. The general significance of the variation of the 6.2/7.7 μm is discussed on Draine & Li (2001). Assumptions about the stellar radiation intensity, which affect the 11.3/7.7 μm ratio as well, account for these variations in the number of C atoms. Following Draine & Li (2001), our observed

ratios correspond to a number of carbon atoms in a PAH grain between 100 and 140 ($6.2/7.7 \mu\text{m} \sim 0.3$) and 240 and 320 ($6.2/7.7 \mu\text{m} \sim 0.2$).

However, there is no correlation between the $6.2/7.7 \mu\text{m}$ ratio with radiation hardness (symbols in Fig. 10) or with any other resolved spatial structure in the central region. Since the variations are comparable to the uncertainties in the measurement, the results are not (yet) significant enough to support PAH size variations at parsec scales. Similarly, the variations of the $11.3/7.7 \mu\text{m}$ ratio are mostly due to extinction and show little support for variations in PAH ionization throughout the region. However, if PAH sizes did vary on parsec scales, one would expect strong emission from the larger grains, which radiate predominantly at larger wavelengths, such as the $17 \mu\text{m}$ complex.

4.4.2. The $17 \mu\text{m}$ PAH Complex

The $16\text{--}18 \mu\text{m}$ wavelength range contains the $\text{H}_2 S(1) 17.03 \mu\text{m}$ line and the $17 \mu\text{m}$ PAH complex. This complex is attributed to a blend of emission features (16.45 , 17.03 , and $17.37 \mu\text{m}$), which are possibly due to PAH C–C bending modes (e.g., Van Kerckhoven et al. 2000), and emission from PAH clusters, amorphous carbon particles, and other PAH-related species (Peeters et al. 2004a). Following the Draine & Li (2007) models, the $17 \mu\text{m}$ complex is mostly emitted by large PAH molecules with 1000–2000 carbon atoms, while the $6.2 \mu\text{m}$ feature is emitted mostly by smaller PAH molecules with only 200–300 carbon atoms. The relatively narrow features at 16.45 and $17.37 \mu\text{m}$ have been detected by *ISO* in Galactic (Moutou et al. 2000) and extragalactic sources (Sturm et al. 2000). Only with the *Spitzer* IRS has the whole $17 \mu\text{m}$ PAH complex been identified and routinely detected in both normal and starburst galaxies (e.g., Smith et al. 2004; Dale et al. 2006; Brandl et al. 2006), including the outer regions of M82 (Engelbracht et al. 2006). However, the spatial variation within galaxies other than the Milky Way has not yet been studied. Engelbracht et al. (2006) detected this complex in the disk and in the halo of M82, but their spectral coverage did not include the central regions. Here we report the characteristics of this complex in the central kpc of M82.

As seen in Table 3 the ratios between the $17 \mu\text{m}$ complex and the $11.3 \mu\text{m}$ PAH feature, as measured with PAHFIT, range from 0.39 in regions 1 and 3 to 0.49 in the center region, and they do not show clear spatial correlations. However, the $17/6.2 \mu\text{m}$ ratio varies from 0.21 in region 3 to 0.57 in region 4. The ratios between the regions in the plane and the outward regions vary by a factor of 2. The latter numbers suggest a significant variation, possibly due to different PAH sizes. However, correcting for an optical depth of $\tau_{9.8} = 2$ for the regions around the $[\text{Ne II}]$ peaks (Fig. 7), the ratio increases by $\sim 67\%$, yielding values of 0.37 for region 2 and 0.35 for region 3. While substantially increased, the values are still more than 20% below the values for regions 1 and 4. However, due to uncertainties on the determination of $\tau_{9.8}$ we cannot diagnose any variation of PAH sizes based on this difference.

Figure 11 shows a baseline-subtracted spectrum of the $17 \mu\text{m}$ PAH complex normalized to the average flux between 16.2 and $17.6 \mu\text{m}$ and rebinned to $R = 300$ to enhance the broad components. In this figure we can see the flux variation in these three main PAH features between the regions. The differences in the strength of these features are consistent within the uncertainties, with exceptions being region 4 at $16.45 \mu\text{m}$ and regions 2 and 3 at $17.37 \mu\text{m}$. Moreover, these discrepancies could be explained by errors in baseline subtraction, which are in the order of 10%. The $17 \mu\text{m}$ PAH complex is also seen in the LL spectra as far as 2 kpc from the galactic plane. The model of Draine & Li (2007)

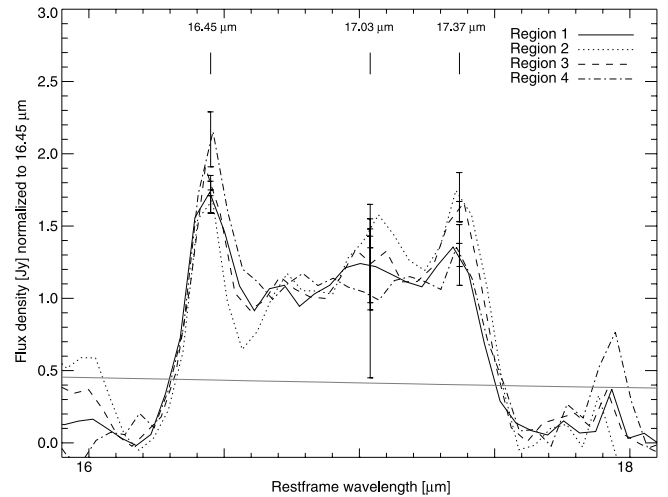


FIG. 11.—Zoom-in on the PAH-dominated emission features in the $16\text{--}18 \mu\text{m}$ spectral range of the SH spectra. The spectra were normalized to the average flux between 16.2 and $17.6 \mu\text{m}$ and rebinned to a resolution $R = 300$, to diminish the noise. The error bars indicate noise at three wavelengths.

predicts that the relative strength of the individual components is not sensitive to ionization state or grain size. Our observations are in good agreement with an invariant shape of this PAH complex.

4.4.3. The Difference between PAH Emission and VSG Emission

Very small grains (VSGs) are dust particles larger on average than PAHs, with typical sizes in the range of $1\text{--}150 \text{ nm}$ (Desert et al. 1990). They are excited by stochastic heating and are thought to be responsible for most of the mid-infrared continuum emission. The properties of these grains in relation to PAHs have been studied previously in galactic sources (Verstraete et al. 1996; Lebouteiller et al. 2007) and in dwarf galaxies (Madden et al. 2006; Wu et al. 2006). These studies focus on the behavior of VSGs in conditions in which PAHs are destroyed, mainly by intense stellar radiation in H II regions or a low-metallicity environment. Flux differences between VSGs and PAHs are reported in Galactic H II regions by (e.g., Lebouteiller et al. 2007), where the PAH/VSG emission ratio increases with the distance from the cluster.

As shown in Table 3, there are significant differences in the EWs of the PAH features between the regions in the galactic plane and the regions outside the galactic plane. However, the EW shortward of $10 \mu\text{m}$ behaves differently from the EW longward of $10 \mu\text{m}$. Longward of $10 \mu\text{m}$, we observe that the EWs of the PAH features increase outward from the galactic plane. The $11.3 \mu\text{m}$ EW, for example, increases from $0.660 \mu\text{m}$ in region 2 to $2.27 \mu\text{m}$ in region 1. The EWs of the 6.2 and $7.7 \mu\text{m}$ decrease outward from the galactic plane. For example, the $6.2 \mu\text{m}$ EW decreases from $1.10 \mu\text{m}$ in region 2 to $0.308 \mu\text{m}$ in region 1. The EW of the $8.6 \mu\text{m}$ feature decreases up to a factor of 2, from $0.865 \mu\text{m}$ in region 3 to $0.437 \mu\text{m}$ in region 2. This could be due to the contribution of the stellar continuum to the local continuum shortward of $10 \mu\text{m}$. The stellar continuum contribution decreases with wavelength and with the distance from the galactic plane.

The continuum longward of $10 \mu\text{m}$ is composed of thermal emission from VSGs. As the PAH flux does not increase outward from the galactic plane, this can only be due to a decrease of the local continuum emission relative to the PAH strength. This decrease can be explained by several different factors: photodestruction, abundance differences between VSGs and PAHs, and

different heating opacities between VSGs and PAHs with a varying radiation field.

Decreasing PAH flux with the hardening of the radiation has been observed in galactic star-forming regions (Verstraete et al. 1996; Lebouteiller et al. 2007), on small spatial scales near the luminous clusters (~ 2 pc), where the PAH destruction largely surpasses PAH excitation. Whether the conditions that lead to PAH destruction on 2 pc scales can be maintained over much larger scales, corresponding to the resolution of our maps (~ 35 pc), cannot be derived from our data but has been observed in NGC 5253 (Beirão et al. 2006). Using the SINGS sample of galaxies, Draine et al. (2007) have shown that the fraction of PAH abundance over the total dust abundance decreases with metallicity. Hence, abundance differences between PAHs and VSGs could be observed in cases of a strong metallicity gradient. M82 has a metallicity gradient, but it becomes noticeable only at distances larger than 1 kpc from the center (Ranalli et al. 2006), which is greater than the distance from our regions 1 and 4 to the galactic plane (400 pc).

Our favored explanation is the difference in excitation between PAHs and VSGs, enhanced by variations of the radiation field. The mid-infrared PAH features are produced by vibrational-rotational modes of the PAH molecules, while the VSG continuum emission is mainly produced by thermal radiation. VSGs are bigger than PAHs, so thermal radiation becomes dominant over vibrational-rotational transitions. Following Draine & Li (2001) models, the opacity of the cross-section peaks at FUV wavelengths, where hot dust is needed to emit at $10\text{--}20\ \mu\text{m}$. However, at the distance from the galactic plane of regions 1 and 4, the radiation field is still intense enough to excite PAHs but no longer of a high enough intensity to excite the dust to the same temperatures as in the plane of the galaxy. This provokes the PAH EW enhancement observed in these regions.

4.5. Excitation of the Warm H_2

Molecular hydrogen is the most abundant molecule in the universe and can be used to probe the properties of the warm molecular gas in M82. It can be traced in the mid-infrared through rotational emission lines, which may arise through three different mechanisms: UV excitation in PDRs surrounding or adjacent to the H II regions; shocks that accelerate and modify the gas in a cloud, collisionally exciting the H_2 molecules; or hard X-ray photons capable of penetrating the molecular clouds and heating large ionizing columns of gas.

Vibrational-rotational H_2 line emission in M82 was studied in the near-infrared by Pak et al. (2004). By correlating the emission flux from these lines with $[\text{C II}]$ $157\ \mu\text{m}$ and far-infrared luminosity, they showed that the H_2 emission comes mainly from the PDRs. *ISO* observations of M82 detected $S(0)$, $S(1)$, $S(2)$, $S(6)$, and $S(7)$ rotational lines (Rigopoulou et al. 2002), excited by UV radiation from massive stars.

The $S(1)$ and $S(2)$ rotational transition lines of H_2 are clearly detected in our SH spectra. The fluxes and temperatures of these lines are listed in Table 2, along with the $S(1)/S(2)$ ratios. The temperatures were calculated from the $S(1)/S(2)$ ratios using the method described by Roussel et al. (2006) assuming an ortho- to para- ratio of 3. Our derived temperatures are in agreement with the average temperature value of 450 K, derived with *ISO* (Rigopoulou et al. 2002). The $\text{H}_2 S(0)$ line could not be detected in any of the LH spectra, as its equivalent width is very low, supporting our finding that the H_2 temperature is indeed relatively high.

If H_2 emission is excited mainly by UV radiation in PDRs, the fluxes of H_2 lines and PAH lines should correlate closely, since

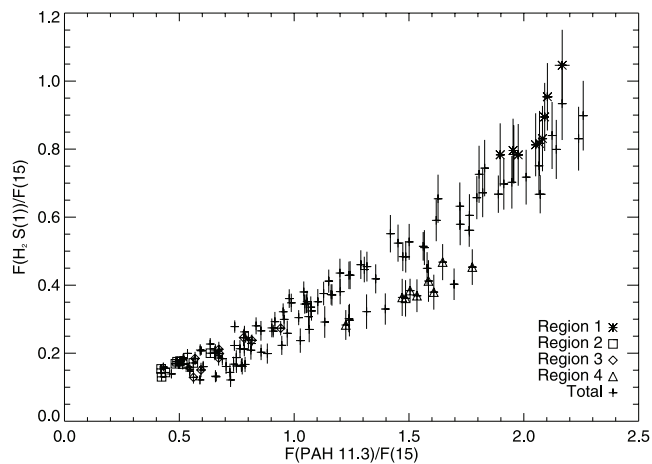


FIG. 12.—PAH $11.3\ \mu\text{m}$ feature over the $15\ \mu\text{m}$ continuum vs. $\text{H}_2 S(1)$ over the $15\ \mu\text{m}$ continuum, based on a pixel-by-pixel correlation between SH maps. The values corresponding to each of the selected regions are represented by different symbols. The error bars represent line flux measurement errors.

PAH emission features arises from the same mechanism in PDRs. To look for secondary effects, such as shocks, we plot in Figure 12 the PAH $11.3\ \mu\text{m}$ versus $\text{H}_2 S(1)$ $17.03\ \mu\text{m}$ fluxes, both divided by the continuum flux at $14.8\text{--}15.2\ \mu\text{m}$ to reduce the range covered by the figure. Each data point corresponds to a resolution element of the CUBISM flux maps taken from SH spectra. The stars correspond to region 1, squares to region 2, diamonds to region 3, and triangles to region 4. The error bars represent the line uncertainties from the measurement. The correlation in Figure 12 shows that the excitation mechanisms for both species coincide at least on spatial scales of the resolution of the map, which is 35 pc. While there is a wider dispersion of data points corresponding to regions 1 and 4 (the regions associated with outflows), the systematic measurement errors account largely for this dispersion. We conclude that shocks in the outflow regions have no measurable influence on the H_2 emission. However, we cannot distinguish between UV and local shock excitation, as produced by supernovae or energetic outflows, on scales smaller than the resolution of our pixels (35 pc).

5. CONCLUSION

We presented spatially resolved mid-infrared spectra of the central region of M82. The spectra were taken with the *Spitzer* Infrared Spectrograph in both the $5\text{--}38\ \mu\text{m}$ low-resolution ($R \sim 65\text{--}130$) and the $10\text{--}37\ \mu\text{m}$ high-resolution $R \sim 600$ module. The high signal-to-noise ratio and the continuous spatial and spectral coverage allowed us to study the nucleus of a starburst galaxy in unsurpassed detail. Our goal was to study the physical conditions of the interstellar medium and their spatial variations within the central kpc of M82.

Overall, the spectra show the typical features of a starburst: prominent PAH features, silicate absorption, fine-structure lines, and a steeply rising continuum. We built a spectral map with high-resolution spectra, selected six representative regions for spectral extraction, and studied the variations of the neon ionic lines and PAH feature emission among the regions.

We attempted to trace the structure of the ionizing radiation, and therefore the young stellar population of M82, through the diagnostic emission lines $[\text{Ne II}]$ $12.8\ \mu\text{m}$ and $[\text{Ne III}]$ $15.5\ \mu\text{m}$. The overall morphology of the ionizing radiation in the region as revealed by the spectral maps appears to be in agreement with previous ground-based observations (Achtermann & Lacy 1995). There is surprisingly little spatial variation of the $[\text{Ne III}]/[\text{Ne II}]$

ratio across the disk, and it varies only by a factor of 3 throughout the central region, with these variations not corresponding to the position of the emission peaks. We observed an increase of the $[\text{Ne III}]/[\text{Ne II}]$ ratio by a factor of 2 outward from the galactic plane, which may be associated with the outflows. We suggest that the increase of the $[\text{Ne III}]/[\text{Ne II}]$ ratio with distance to the galactic plane is due to a decrease in gas density rather than a hardening of the field.

The $[\text{Ne III}]/[\text{Ne II}]$ ratio is low on average, which indicates that the dominant population consists of already evolved clusters (>5 Myr). We cannot rule out the presence of ongoing star formation in the central region, but it must occur at a much reduced rate ($<5\%$) compared to previous epochs. This drop is unlikely to be caused by starvation, as there is still a large amount of molecular gas present in the central region. It is more likely due to negative feedback processes causing a decrease in the star formation rate.

There are significant variations in the amount of dust extinction, which strongly correlate with the CO 1–0 emission across the central region. These variations are strong enough to affect the interpretation of PAH features, but due to limited spectral coverage the extinction estimates are uncertain.

The flux of the main PAH features correlates spatially with the flux of the neon ionic lines, and with previous IRAC observations. Variations in the PAH ratios such as $6.2/11.3 \mu\text{m}$ were observed across the disk. However, they are strongly affected by the silicate feature at $10 \mu\text{m}$. We studied the variations the $6.2/7.7 \mu\text{m}$ and $11.3/7.7 \mu\text{m}$ PAH ratios, which are diagnostics for the size and the degree of ionization of PAHs. We found no correlation between the $6.2/7.7 \mu\text{m}$ ratio with radiation hardness or with any other resolved spatial structure in the central region. Since the variations are comparable to the uncertainties in the measurement, the results are not (yet) significant enough to support PAH size variations at parsec scales. Similarly, the variations of the $11.3/7.7 \mu\text{m}$ ratio are mostly due to extinction and show little support for variations in PAH ionization throughout the region.

The $17 \mu\text{m}$ PAH complex is very prominent in the center of M82. We did not find any relative variations within the complex, which is in agreement with predictions. The variations of the $17/6.2 \mu\text{m}$ ratio are most likely due to extinction effects. Due to the uncertainties in the determination of extinction, we did not

consider the remaining variations as a clear indicator of PAH size variation.

We observed an enhancement of the EWs of the $11.3 \mu\text{m}$ and the other PAH features longward of $10 \mu\text{m}$ outward from the galactic plane. Several explanations exist for this, but we favor the variation of the UV radiation field, which excites differently PAHs and VSGs, given their different sizes.

The $S(1)$ and $S(2)$ rotational transition lines of H_2 have been detected in our spectra throughout the central region. H_2 and PAHs coincide at least on spatial scales of the resolution of the map, which is 35 pc. We conclude that large-scale shocks in the outflow regions have no measurable influence on the H_2 emission. However, we cannot distinguish between UV and local shock excitation as produced by supernovae or energetic outflows, on scales smaller than the resolution of our pixels (35 pc).

The *Spitzer* IRS observations of the central region of M82 complements previous studies, not only in mid-infrared, but also in other wavelengths. Our results demonstrate the importance of spatially resolved spectroscopy in starburst studies. They helped to constrain the age of the starburst and confirm results from other studies and also stressed the importance of a thorough study of extinction to investigate possible variations of PAH properties. Further research of the starburst feedback and quenching processes will elucidate the sharp decrease in star formation in the last 5 Myr. It would be interesting to see if higher spatial resolution, as expected from the MIRI on board the *James Webb Space Telescope (JWST)* will discover a wider variation of the radiation field or signs of variation of PAH sizes and/or ionization. In addition, spatially more extended spectral studies of M82 are necessary to study the connection of the ionic line ratios with the outflows.

We would like to thank L. Snijders for making the Starburst99+ Mappings models available. We would like to thank J. Lacy for providing the mid-infrared maps from IRTF ground-based observations. We also thank the anonymous referee, whose many thoughtful and useful comments greatly improved this paper. This work is based on observations made with the *Spitzer Space Telescope*, which is operated by the Jet Propulsion Laboratory, California Institute of Technology, under NASA contract 1407.

REFERENCES

- Achtermann, J. M., & Lacy, J. H. 1995, *ApJ*, 439, 163
 Alton, P. B., Davies, J. I., & Bianchi, S. 1999, *A&A*, 343, 51
 Appleton, P. N., Davies, R. D., & Stephenson, R. J. 1981, *MNRAS*, 195, 327
 Beirão, P., Brandl, B. R., Devost, D., Smith, J. D., Hao, L., & Houck, J. R. 2006, *ApJ*, 643, L1
 Brandl, B. R., et al. 2006, *ApJ*, 653, 1129
 Bregman, J. N., Schulman, E., & Tomisaka, K. 1995, *ApJ*, 439, 155
 Cappi, M., et al. 1999, *A&A*, 350, 777
 Chiar, J. E., & Tielens, A. G. G. M. 2006, *ApJ*, 637, 774
 Colbert, J. W., et al. 1999, *ApJ*, 511, 721
 Dale, D. A., et al. 2006, *ApJ*, 646, 161
 de Grijs, R., O'Connell, R., & Gallagher, J. S. 2001, *AJ*, 121, 768
 Desert, F.-X., Boulanger, F., & Puget, J. L. 1990, *A&A*, 237, 215
 Draine, B. T., & Li, A. 2001, *ApJ*, 551, 807
 ———. 2007, *ApJ*, 657, 810
 Draine, B. T., et al. 2007, *ApJ*, 663, 866
 Engelbracht, C. W., et al. 2006, *ApJ*, 642, L127
 Förster Schreiber, N. M., Genzel, R., Lutz, D., Kunze, D., & Sternberg, A. 2001, *ApJ*, 552, 544
 Förster Schreiber, N. M., Genzel, R., Lutz, D., & Sternberg, A. 2003a, *ApJ*, 599, 193
 Förster Schreiber, N. M., Sauvage, M., Charmandaris, V., Laurent, O., Gallais, P., Mirabel, I. F., & Vigroux, L. 2003b, *A&A*, 399, 833
 Freedman, W. L., & Madore, B. F. 1988, *ApJ*, 332, L63
 Heckman, T. M., Lehnert, M. D., Strickland, D. K., & Armus, L. 2000, *ApJS*, 129, 493
 Higdon, S. J. U., et al. 2004, *PASP*, 116, 975
 Hoopes, C. G., et al. 2005, *ApJ*, 619, L99
 Houck, J. R., et al. 2004, *ApJS*, 154, 18
 Huggins, D. M., & Allamandola, L. J. 1995, *J. Phys. Chem.*, 99, 3033
 Joblin, C., Tielens, A. G. G. M., Geballe, T. R., & Wooden, T. H. 1996, *ApJ*, 460, L119
 Kronberg, P. P., Biermann, P., & Schwab, F. R. 1985, *ApJ*, 291, 693
 Larkin, J. E., Graham, J. R., Matthews, K., Soifer, B. T., Beckwith, S., Herbst, T. M., & Quillen, A. C. 1994, *ApJ*, 420, 159
 Lebouteiller, V., Brandl, B., Bernard-Salas, J., Devost, D., & Houck, J. R. 2007, *ApJ*, 665, 390
 Lehnert, M. D., Heckman, T. M., & Weaver, K. A. 1999, *ApJ*, 523, 575
 Lipsy, S. J., & Plavchan, P. 2004, *ApJ*, 603, 82
 Lo, L. Y., Cheung, K. W., Masson, C. R., Phillips, T. J., Scott, S., & Woody, D. P. 1987, *ApJ*, 312, 574
 Madden, S., Galliano, F., Jones, A. P., & Sauvage, M. 2006, *A&A*, 446, 877
 Mayya, Y. D., Carrasco, L., & Luna, A. 2005, *ApJ*, 628, L33
 Moutou, C., Verstraete, L., Léger, A., Sellgren, K., & Schmidt, W. 2000, *A&A*, 354, L17
 Muxlow, T. W. B., Pedlar, A., Wilkinson, P. N., Axon, D. J., Sanders, E. M., & de Bruyn, A. G. 1994, *MNRAS*, 266, 455
 Pak, S., Jaffe, D. T., Stacey, G. J., Bradford, C. M., Klumpe, E. W., & Keller, K. D. 2004, *ApJ*, 609, 692

- Pauldrach, A. W. A., Lennon, M., Hoffmann, T. L., Sellmaier, F., Kudritzki, R.-P., & Puls, J. 1998, in ASP Conf. Ser. 131, Properties of Hot Luminous Stars, ed. I. Howarth (San Francisco: ASP), 258
- Peeters, E., Mattioda, A. L., Hudgins, D. M., & Allamandola, L. J. 2004a, ApJ, 617, L65
- Peeters, E., Spoon, H. W. W., & Tielens, A. G. G. M. 2004b, ApJ, 613, 986
- Ranalli, P., Origlia, L., Comastri, A., Maiolino, R., & Makishima, K. 2006, in The X-Ray Universe, ed. A. Wilson (ESA SP-604; Noordwijk: ESA), 839
- Rieke, G. H., & Lebofsky, M. J. 1985, ApJ, 288, 618
- Rigopoulou, D., Kunze, D., Lutz, D., Genzel, R., & Moorwood, A. F. M. 2002, A&A, 389, 374
- Roussel, H., et al. 2006, ApJ, 646, 841
- Satyapal, S., Watson, D. M., Pipher, J. L., Forrest, W. J., Greenhouse, M. A., Smith, H. A., Fischer, J., & Woodward, C. E. 1997, ApJ, 483, 148
- Shen, J., & Lo, L. Y. 1995, ApJ, 445, L99
- Shopbell, P. L., & Bland-Hawthorn, J. 1998, ApJ, 493, 129
- Smith, J. D., et al. 2004, ApJS, 154, 199
- . 2007a, PASP, 119, 1133
- . 2007b, ApJ, 656, 770
- Smith, L. J., Westmoquette, M. S., Gallagher, III, J. S., O'Connell, R. W., Rosario, D. J., & de Grijs, R. 2006, MNRAS, 370, 513
- Snijders, L., Kewley, L., & van der Werf, P. 2007, ApJ, 669, 269
- Spoon, H. W. W., Marshall, J. A., Houck, J. R., Elitzur, M., Hao, L., Armus, L., Brandl, B. R., & Charmandaris, V. 2007, ApJ, 654, L49
- Strickland, D. K., Heckman, T. M., Colbert, E. J. M., Hoopes, C. G., & Weaver, K. A. 2004, ApJS, 151, 193
- Strickland, D. K., Ponman, T. J., & Stevens, I. R. 1997, A&A, 320, 378
- Sturm, E., Lutz, D., Tran, D., Feuchtgruber, H., Genzel, R., Kunze, D., Moorwood, A. F. M., & Thornley, M. D. 2000, A&A, 358, 481
- Sun, W.-H., et al. 2005, ApJ, 630, L133
- Telesco, C. M., Joy, M., Dietz, K., Decher, R., & Campins, H. 1991, ApJ, 369, 135
- Thornley, M. D., Förster Schreiber, N. M., Lutz, D., Genzel, R., Spoon, H. W. W., Kunze, D., & Sternberg, A. 2000, ApJ, 539, 641
- Turner, J. L., Beck, S. C., Crosthwaite, L. P., Larkin, J. E., McLean, I. S., & Meier, D. S. 2003, Nature, 423, 621
- Van Kerckhoven, C., et al. 2000, A&A, 357, 1013
- Vermeij, R., Peeters, E., Tielens, A. G. G. M., & van der Hust, J. M. 2002, A&A, 382, 1042
- Verstraete, L., Puget, J. L., Falgarone, E., Drapatz, S., Wright, C. M., & Timmermann, R. 1996, A&A, 315, L337
- Walter, F., Weiss, A., & Scoville, N. 2002, ApJ, 580, L21
- Wu, Y., Charmandaris, V., Hao, L., Brandl, B. R., Bernard-Salas, J., Spoon, H. W. W., & Houck, J. R. 2006, ApJ, 639, 157
- Yun, M. S., Ho, P. T. P., & Lo, K. Y. 1993, ApJ, 411, L17
- . 1994, Nature, 372, 530